43rd AIAA Aerospace Sciences Meeting and Exhibit, 10-13 Jan 2005, Reno, Nevada

Modeling Surface Discharge Effects of Atmospheric RF on Gas Flow Control

Subrata Roy[*]
Computational Plasma Dynamics Laboratory, Kettering University, Flint, MI 48504, USA

and

Datta V. Gaitonde[†]
Computational Sciences Branch, Air Force Research Laboratory, Wright Pat AFB, Ohio 45433, USA

The advantages of plasma actuators for flow control are being increasingly recognized in the literature in all speed regimes encountered in aerospace applications. Recent experiments with suitably configured atmospheric RF discharges have demonstrated particularly striking effects by reducing or eliminating separation in low-speed flows. In this paper, a finite-element multi-fluid formulation is developed and utilized to model the RF induced plasma dynamics of an asymmetric electrode configuration. Partially ionized helium gas flow is considered over two electrodes, one exposed and one embedded in a thin dielectric material. The exposed electrode is powered with an RF potential and the embedded electrode is considered grounded. In a previous work, the derived electric field for a discharge between two insulated electrodes was coupled to a simple phenomenological model for the transverse velocity in a one-dimensional situation that predicted the anticipated hump in the near wall profile. Here the model is modified for the surface barrier discharge, extended to two-dimensions and applied to a realistic configuration comprised of a flush-mounted surface electrode and a corresponding streamwise displaced electrode embedded in the dielectric. The results extract features of the plasma-wall interaction on the neutral flow field with a self-consistent approach. The computed solutions for the evolution of electric field, space charge distribution and neutral gas densities are presented. The effect of the electric force due to surface discharge on the working gas flow is also demonstrated.

Nomenclature

A,B	Coefficients
C	Capacitance, farad
D	Diffusion coefficient, cm^2/s
d	Characteristic length, cm
E	Electric field, V/cm
e	Electron charge, coulomb
ε	Permittivity, farad/m
F	Solution residual
ϕ	Potential, V
Γ	Flux, cm^{-2}/s
I	Current, Amp/cm^2
λ_{De}	Electron Debye length, χm
λ_i	Ion mean free path, cm
m	mass, kg
μ	Mobility, cm^{2}V^{-1}s^{-1}
n	Number density, cm^{-3}
ω	Applied frequency, radians
Ω	Computational domain
p	Pressure, Pa
r	Recombination coefficient

---

[*] Associate Professor of Mechanical Engineering, 1700 West Third Avenue, and AIAA Associate Fellow.

[†] Technical Area Leader, Air Vehicles Directorate/VAAC, 2210 8th St., and AIAA Associate Fellow.

S	Ionization frequency, s^{-1}
T	Temperature, eV
t	Time coordinate, s
V	Species velocity, m/s
x	Spatial coordinate, cm
z	ionization rate, /s

Subscripts:

α	Species
B	Bohm
e	Electron, finite element
f	fluid
i	Ion
n	neutral
0	Reference value

I. Introduction

THE use of plasma actuators for flow control is being widely investigated in all speed regimes for aerospace applications. The advantages of these actuators include no moving parts, rapid switch-on/off capabilities, and application of large forces in a relatively precise and controlled manner. These benefits make such approaches particularly suitable for flow control in wall layers or separated layers at both low[1-5] and high speeds.[6,7] Recent experimental efforts[1-3] have successfully demonstrated the flow actuation capability of dielectric barrier discharges (DBDs) to inhibit phenomena such as stall on airfoils, thus improving their lift-drag curves. The mechanism is particularly attractive as it can operate at atmospheric conditions and can limit itself automatically before an uncontrolled macroscopic breakdown. Experimental efforts have identified many of the key parameters, most prominent among which are the geometric configuration, such as the relative location and placement of the electrodes, and the form of the applied excitation.

A broad description of the fluid-plasma interaction may be presented as follows. The electrode arrangement, shown schematically in Figure 1, is such that the insulator surrounds the grounded electrode and a voltage fluctuating at radio frequency (RF) is applied to the electrode exposed to the gas. The parameters employed in experimental observations include peak-to-peak voltage range between 2-20 kV at 1-50 kHz RF*,* which are suitable for actuation at atmospheric pressure. At this pressure, the gas is highly collisional, yielding an efficient momentum exchange between charged and neutral species. A complex unsteady interaction occurs between the two electrodes, details of which depend on frequency, voltage, geometric configuration and dielectric constants of the media. As the applied voltage becomes sufficiently large for a given interelectrode distance, a discharge appears with features of a DBD, which weakly ionizes the near-wall gas. The combination of electrodynamic and collisional processes whose detailed mechanics is yet to be understood, ultimately results in transfer of momentum acquired from the electric field by the charged particles to the neutrals which are the primary species. The asymmetry in the location of the electrodes, coupled with the phase shift of the electrode when multiple devices are present, yields directional macroscopic effects on the bulk gas.

Capacitively coupled atmospheric RF glow discharges have been reported by many researchers.[8-11] Although the glow appears to be homogeneous, close inspection reveals that the discharge may consist of micro sparks. Typically, it is the light emission spectrum that remains diffused to create a uniform glow. It has been observed that in some gases (e.g. helium) the discharge glow is stable, whereas for the same interelectrode gap and pressure air, nitrogen, oxygen and argon transition into an unstable filamentary discharge.[12] The recent experimental success of RF induced DBD using air at atmospheric condition[1,3] thus shows tremendous potential in the areas of electro gas dynamic flow control. In this discharge, microfilaments of nanosecond duration with many current pulses in a half cycle maintain the optical glow. A typical distance between DBD electrodes is ~0.1 mm in plasma displays, over 1 mm in ozone generators, to several cm in CO_2 lasers.[12] Between the two types of DBD, namely volume discharge between two parallel plates and surface discharge over a dielectric boundary, this study focuses on the latter.

In a surface discharge, within a very short time after breakdown, the charge build-up at the dielectric surface sets off microdischarges of nanosecond duration, limiting the electric field at the location of the microdischarge such that the charge current at this position is cut-off. The small timescale of the discharge allows minimal charge transport and energy dissipation, thus resulting in minimal heating of the bulk gas. The electric field energy is mostly utilized to excite the carrier gas particles thus facilitating various applications including boundary layer flow actuation. Several specific configurations have been proposed and tested to exploit the complex interaction between the electric field and the fluid. A detailed discussion may be found in Ref. [1,3].

Despite the recently reported extensive experimental observations on atmospheric DBD interactions for flow actuation, the theoretical modeling effort may be characterized as relatively less mature. The collisional RF sheath dynamics of near-surface regions are fundamentally different than that under direct current (DC) and/or collisionless conditions and substantially more difficult to simulate because of their unsteady nature. Published numerical efforts span a range of phenomenological to rudimentary first principle based methods.[2,4,5,13] For example, Roth[3] utilized a balance between the electrostatic force and the hydrodynamic force to estimate the induced gas velocity. Shyy et al.[5] assumed a triangular distribution of the electrostatic body force downstream of the electrode with a constant charge density and then utilized Navier-Stokes equation to predict its effects on the flow. Enloe et al.[2] have analytically shown in a simple one-dimensional axisymmetric configuration why two dimensional electric force modeling is fundamental to the understanding of the DBD flow actuation process. For accuracy and fidelity, it is essential that the force model be derived from first principles through a simulation of the elementary mechanisms that yield the discharge. Roy and Gaitonde[5] demonstrated such a model for volume discharge between two dielectric coated electrodes using a finite element-based one-dimensional multi-fluid formulation of plasma–sheath for atmospheric conditions. The model was relatively basic but formed the framework of a first principles based methodology. Simulations showed reasonable comparison with reported RF glow discharges[13] in partially ionized helium gas between two insulated electrodes. The current effort is a logical next step in the evolution of computational methods for DBDs.

The goal of this effort is to present the first two-dimensional modeling of collisional surface dielectric barrier discharge at atmospheric pressures with a consistent calculation of charge and neutral number densities, their momentum dynamics, electric field and potential distribution. The formulation is anchored in an efficient, robust and versatile module-based finite-element Multiscale Ionized Gas (MIG) flow code[5,16-19], to facilitate the prediction of the electric field from the charge distribution arising from the configuration, applied RF potentials, properties of the dielectric medium and the gas. The *electric force*, computed as a product of self-consistent charge and electric field, is employed to calculate the flow actuation effect. For simplicity, here again helium is used as a carrier gas because its plasma coefficients and chemistry are known. This will lay the basis for a sophisticated model, with the capability not only to model the physics, but also to do so with a method that is easily extendible to complex configurations to complement experimental efforts in future design and development.

This paper is organized as follows. Section II describes the problem statement. Section III specifies the boundary conditions and the normalization schemes adopted. Section IV explains the methodology used to solve the system of equations. Section V describes and interprets the computed results. Section VI summarizes the conclusions.

II. Problem Statement

The following two-dimensional three species collisional plasma-sheath model is solved.

Charge continuity:

$$\frac{\partial n_\alpha}{\partial t} + \frac{\partial n_\alpha V_{\alpha j}}{\partial x_j} = n_e z - r n_e n_i \tag{1a}$$

Charge momentum:

$$n_\alpha V_{\alpha j} = -\operatorname{sgn}(e) n_\alpha \mu_\alpha \frac{\partial \phi}{\partial x_j} - D_\alpha \frac{\partial n_\alpha}{\partial x_j} \tag{1b}$$

Potential:

$$\varepsilon \left(\frac{\partial^2 \phi}{\partial x_j^2} \right) = e(n_e - n_i) \tag{2}$$

Neutral continuity:

$$\frac{\partial n_n}{\partial t} + \frac{\partial n_n V_{nj}}{\partial x_j} = -n_e z + r n_e n_i \tag{3}$$

The charge particle $\alpha = e,i$ distributions are considered non-Maxwellian and inertia terms are neglected. The electron temperature is nearly uniform at 1eV = 11,600K and the ions and neutrals are in thermal equilibrium at 300K. The working gas, helium, is maintained at bulk pressure p = 300 torr and temperature T = 300K.

Transport properties are taken from the literature. The electron diffusion is obtained from Einstein relation, $D_e = (T_e / e)\mu_e$, where T_e is the energy in electron volts, e is the elementary charge, ε is the permittivity, and $\mu_e = e/(m_e \nu_{eh})$ is mobility of an electron, where $\nu_{en} \approx 10^{12}$/s is the electron-neutral collision frequency.[14] We emphasize that transport properties used from the published literature are to be taken as nominal values facilitating the development of the numerical framework, rather than providing new thermo-chemical data for these discharges. Similarly, the ion diffusion D_i=500 cm^2/s at 300K, and the ion mobility μ_i is given as[15]:

$$
\begin{aligned}
p\mu_i &= 8\times10^3\left(1-8\times10^{-3}E/p\right)\ \text{cm}^2\text{V}^{-1}\text{s}^{-1}\text{torr},\ \text{ for } E/p\le 25\ \text{V cm}^{-1}\text{torr}^{-1} \\
p\mu_i &= \frac{4.1\times10^4}{\sqrt{E/p}}\left(1-\frac{27.44}{\left(E/p\right)^{3/2}}\right)\ \text{cm}^2\text{V}^{-1}\text{s}^{-1}\text{torr},\ \text{ for } E/p > 25\ \text{V cm}^{-1}\text{torr}^{-1}
\end{aligned}
\qquad (4)
$$

where $E=\sqrt{E_x^2+E_y^2}$ is the electric field magnitude with components $E_j=-\partial\phi/\partial x_j$ and p is the gas pressure. The index j takes the values x and y. The ionization rate z for helium gas used here is from Ref. 5:

$$
z = \text{A}\exp\left(\frac{-\text{B}}{\left(E/p\right)^{0.4}}\right)p\mu_e E\ \ \text{s}^{-1};\quad \text{A} = 4.4\ \text{cm}^{-1}\text{torr}^{-1}\ \text{and B} = 14\ [\text{V/(cm torr)}]^{0.4} \qquad (5)
$$

where, n_e is the electron number density. The coefficient of recombination on the right hand side of Eqn. (1a) and (3) is given as[17], $r=\left\langle V_{\text{eth}}\sigma_{ei}^{r}\left(V_{\text{eth}}\right)\right\rangle = 1.09\times10^{-20}T^{-9/2}n_e$ m^3/s. Here, V_{eth} is the electron thermal velocity and σ_{ei} is the electron-ion collision cross-section. For simplicity, we have presently ignored recombination effect on momentum, as well as secondary emission, at this stage.

The dynamics of neutral particles are determined using the following neutral momentum equations:

$$
\frac{\partial V_{nj}}{\partial t}+V_{nl}\frac{\partial V_{nj}}{\partial x_l}=\frac{\varpi}{m_n n_n}\frac{\partial}{\partial x_j}\left[\varepsilon\left(\frac{\partial\phi}{\partial x_l}\right)^2\right]+\frac{m_e n_e}{m_n n_n}\nu_{en}\left(V_{ej}-V_{nj}\right)+\frac{Mn_i}{m_n n_n}\nu_{in}\left(V_{ij}-V_{nj}\right)+n_e z V_{ij}/n_n \qquad (6)
$$

The averaged velocity of the fluid of density $\rho\approx m_n\left(n_n+n_i\right)$ is based on the following momentum equation:

$$
\frac{\partial V_{fj}}{\partial t}+V_{fl}\frac{\partial V_{fj}}{\partial x_l}=\frac{\varpi}{\rho}e\left(n_i-n_e\right)E_j-\frac{\text{R}T}{\rho}\frac{\partial\rho}{\partial x_j}+\frac{\partial}{\partial x_l}\tau_{jl}\ , \qquad (7)
$$

where $\tau_{jl}=\frac{\mu}{\rho}\left(\frac{\partial V_{fl}}{\partial x_j}+\frac{\partial V_{fj}}{\partial x_l}\right)-\frac{2}{3}\frac{\mu}{\rho}\frac{\partial V_{fk}}{\partial x_k}\delta_{jl}$ with μ as the gas viscosity ($=2.066\times10^{-5}$ Ns/m^2) and δ_{jl} is the Kronecker delta. The factor ϖ introduced to modulate the effect of electric field is set to unity.

The multiscale ionized gas (MIG) flow code was used to solve Eqns. (1)-(7). MIG implements a versatile high-fidelity finite-element (FE) procedure adapted from fluid dynamics to overcome the stiffness of the equations generated by multi-species charge separation phenomena.[5,16-18] FE techniques are especially suitable for their adaptability to arbitrary multidimensional geometries and boundary conditions. Here, a 2D bilinear finite element formulation is employed together with 4th order Runge-Kutta time marching to solve the continuity and momentum equations for all species and fluid. The solution process consists of two steps. First, using Eqns. (1a), (2), (3) and (6), a global matrix is formed and solved simultaneously obviating the need for any special sub-iteration for the Poisson solver. The species density and charge velocity thus calculated are then used in Eqn. (7) to predict the fluid velocity. The Galerkin weak statement associated with a variational integral underlines the development of this numerical algorithm. The solution of the Newton iteration is converged at any given timestep when the maximum value of the residual, relative norm for each of the state variables, becomes smaller than a chosen convergence criterion of 10^{-4}.

III. Boundary Conditions

The computational domain (x,y: 0,0.01m) consists of a lower half (y:0,0.005m) insulator with dielectric constant ε_d= 4.5 ε_0, and a upper half filled with inert helium gas of ε_f= 1.0055 ε_0 where ε_0 is permittivity of vacuum. Inside the insulator the current due to motion of charged particles is forced to zero while the displacement current is balanced with the total current at the gas-dielectric boundary. The schematic in Figure 1 shows two electrodes in which the bottom electrode is grounded, $\varphi(0)$= 0, and a sinusoidal RF alternating potential $\varphi_{rf}=\varphi_{rms}\sin 2\pi f t$ with φ_{rms}=1 kV and f=5 kHz is applied to the top electrode. Each electrode is infinitesimally thin and 2mm long.

In order to identify the effect of geometric configuration two different electrode arrangements were simulated. In the first, the two electrodes were kept vertically aligned. Hereafter, we will denote this as the symmetric configuration. In the second case, the electrodes are offset horizontally by 2mm. This will be noted as the asymmetric configuration. A decrease in the offset horizontally and/or vertically increases the electric field for the same applied rms potential which in effect increases induced electric force. For all simulations electrons are assumed to be isothermal at the boundary and maintained at 1eV (~11,600K) while the ions are cold (300K) at 300 torr. The electron flux at the exposed electrode is based on the electron thermal velocity and is directed towards the wall. Homogeneous Neumann boundary condition ($\partial n_i/\partial x=0$) is imposed for ions at the exposed electrode. The solutions are verified by qualitative comparison with published results. The simulations are then employed to explore the enhancement of near wall fluid velocity.

IV. Methodology

The ionized helium gas is numerically modeled using the finite-element based MIG flow code. The code is modular and separate subroutines can be written to model different physics. Here, the equation sets (1) – (6) can be written with operator L as L (**q**) = 0 where **q** contains state variables like number densities, velocities and potential. Multiplying with a permissible test function η and integrating over the spatially discretized domain Ω, the variational statement results in the weak form[20]

$$WS^h = \Im_e \left(\int_{\Omega_e} \left[\eta L(\boldsymbol{q}) d\tau \right] \right)_e = 0$$

for a discretization h of $\Omega = \bigcup \Omega_e$ and $\Im_e$ is the non-overlapping sum over the elements. Thus, for example, the GWS form of Eq. (2) becomes,

$$\sum_e \left(\int_{\Omega_e} \frac{d\eta}{dz}\frac{d\eta^T}{dz} dz\{\phi\}_e + \int_{\Omega_e} \eta\eta^T dz\{n_e\}_e - \int_{\Omega_e} \eta\eta^T dz\{n_i\}_e - \int_{\Omega_e \cap \partial\Omega_e} \eta \frac{d\eta^T}{dz} dz\{\phi\}_e = F_\phi \right)_e \qquad (8)$$

where F_ϕ is the solution residual.

The Jacobian matrix $J=[\partial F/\partial \boldsymbol{q}]$ in the global $[J].\{\partial \boldsymbol{q}\} = -\{F\}$ is resolved using LU-decomposition scheme for updating change in discretized solution vector **q** at each iteration. The terminal non-linear ordinary differential equation (ODE) systems are solved using implicit Euler method for temporal evolution and N-R iterative algorithm for the non-linear matrix algebra. The convergence criterion for all variables at any iteration is set at 10^{-4}. Solution stability is ensured by appropriate selection of time marching step size and the introduction of artificial diffusion.

V. Results and Discussion

Figures 2 and 3 display several features of the solution on both the symmetric and asymmetric configurations. Figure 2a shows the axial electric field contours with embedded electric field lines computed for the symmetric configuration (at ~ π/2 radians). The electric field lines trace the vector path moving in a trajectory from the exposed instantaneous anode to the grounded cathode inside the dielectric in a symmetric fashion. The ions travel along these repelling field lines of equal strength pushing outward from the center above the RF electrode inducing the neutral gas particles to follow suit. The net effect is clearly seen in the streamwise gas velocity contours in Figure 2b calculated from the electric field depicting counteracting flow field that reduces the neutral gas density in the region above the exposed (RF) electrode. An interesting outcome is that the fluid over the electrode will respond to this pulsating field by forming a jet, whose oscillations will depend on fluid inertia and the instantaneous polarity.

However, this characteristic behavior changes when the embedded electrode is displaced axially relative to the exposed electrode. Figure 3a plots the instantaneous (at ~ π/2 radians) axial electric field distribution for an exposed anode and a grounded cathode in asymmetric configuration. The magnitude of the axial field shows a large round peak (in red) at the right of the anode and a small negative (in blue) just left of the anode. The electric field lines overlaid on this clearly represent a directional bias towards right. The dominant acceleration of ions occurs towards right along these lines leaving only a relatively smaller regime moving in the opposite direction. The net result is an order of magnitude higher (than the symmetric case) gas velocity downstream of the right edge of the exposed anode with a two orders of magnitude smaller negative velocity near the left edge. These results stress that the asymmetry enhances the electric field and thus influences flow direction (cf. Ref. [2]).

A clearer understanding of the asymmetric configuration may be derived by exploring various quantities at several phases of the excitation. The time evolution of the axial electric field and charge distribution are shown in Figures 4 and 5 for four time stations inside a half-cycle. The potential distribution gradually decays from anode to cathode as the RF electrode potential gradually moves through the positive half cycle. The corresponding axial electric field in Figure 4 shows the development of a near circular growth of positive peak of approximately 1.1×10^5 volts/cm and negative trough of 5.5×10^4 volts/cm at the right and left end of the exposed electrode, respectively. This shows that Shyy et al.'s[4] assumption of triangular distribution of the average electric field is quite rudimentary. The computed solutions are very similar to the experimental data of Corke et al.[1] where the exposed electrode is situated upstream of the peak location of the electric field and thus the peak of velocity. Note that the highest value of the electric field about the edges of the grounded electrode is at least twice as much of that near the exposed electrode. The peak of the crosswise component E_y (not shown here due to space limitation) is however, just above the electrodes. Specifically, above the positive electrode E_y takes values of about 4×10^4 volts/cm.

Based on the Poisson equation (2), the divergence of the electric field is directly related to the charge distribution. Figure 5 displays vertical profiles of space charge downstream of the electrode at various locations and phases of the excitation. The negative charge accumulation at the surface is consistent with the physical model of the DBD for the charge deposition at the surface of the dielectric[12]. The crosswise distribution of charge at 1.5mm and 2mm downstream of the exposed electrode shows the accumulation of electrons over time on the dielectric surface. The electron accumulation forms a secondary electrode in the positive half of the cycle balancing the applied potential in the powered electrode in the negative half of the cycle, thus controlling the formation of unbounded discharge in the form of arcs.

Figure 6a plots streamwise component of the computed gas velocity depicting a strong peak downstream of the RF electrode away from the dielectric surface. The initial condition is zero flow, which makes the computational problem more challenging from a numerical stiffness standpoint. The local vertical line plots at seven streamwise locations, Fig. 6b, describe the response of the flow velocity to the increase in axial electric field (Figure 4). The peak of the wall jet like feature occurs at ~2mm downstream of the exposed electrode beyond which diffusive momentum transfer effect increase the height of the region influenced by the DBD, and the peak velocity diminishes. These results exhibit strong qualitative agreement with the published experimental data[1-3].

VI. Conclusions

A two-dimensional finite element based formulation of plasma–fluid interactions is given for a partially ionized plasma using the multi-component fluid equations. The model is applied to simulate an atmospheric surface dielectric barrier discharge for partially ionized helium gas. The computed results are similar to the experimental data showing the exposed electrode is situated upstream of the peak location of the electric field and thus the imparted fluid momentum. The two-dimensional predictions mimic the bounded discharge mechanism due to the charge accumulation on the insulator surface and the lowest electron current just beyond the peak applied voltage. The results however, stress that the asymmetry enhances the electric field. The effect of insulator dielectric constant in the computed electric field lines shows noticeable decrease in the crosswise electric field, possibly increasing the power requirement. More investigation is needed to ascertain optimum electrical parameters. In the near future, the model will be extended to air with negative ions and additional new mechanisms in the source terms. A model for realistic fully three-dimensional geometric and electrode configuration is also under development, as is an exploration of the effect of different voltage shapes (e.g. saw tooth, square wave etc.). The present effort thus provides a practical tool to augment experimental observations in exploring flow control concepts and in developing suitable inputs for traditional fluid dynamics codes based on the Navier-Stokes equations.

Acknowledgements

This work was partially supported by the Summer Faculty sponsorship of VAAC during the summer of 2004, the NRC/AFOSR research fellowship during the summer of 2003, and the Air Force Research Laboratory contract no. F33615-98-D-3210 and AFOSR grants.

References

[1] T.C. Corke, E.J. Jumper, M.L. Post, et al., AIAA Paper No. 2002-0350, Reno, 2002.
[2] C.L. Enloe, T.E. McLaughlin, R.D. VanDyken, et al., *AIAA J., 42, 595 (2004)..*
[3] J.R. Roth, Phys. Plasmas, **10**, 2117 (2003).
[4] W. Shyy, B. Jayaraman and A. Andersson, J. Appl. Phys., **92**, 6434 (2002).
[5] S. Roy and D. Gaitonde, J. Appl. Phys. **96**, 2476 (2004).
[6] S.O. Macheret, M.N. Shneider, and R.B. Miles, Journal of Propulsion and Power, **18**, 424 (2002).
[7] Y.C. Ganiev, V.P. Gordeev, A.V. Krasilnikov, et al., J. Thermophysics and Heat Transfer, **14**, 10 (2000).
[8] S. Kanazawa, M. Kogoma, S. Okazaki, et al., J. Phys. D: Appl. Phys. **26**, 838 (1988).
[9] D. Liang and M.W. Blades, Spectrochim. Acta Part B, **15**, 1049 (1989).
[10] S.D. Anghel, T. Frentiu, E.A. Cordos, et al., J. Anal. At. Spectrom. **14**, 541 (1999).
[11] R. Guevremont and R.E. Sturgeon, J. Anal. At. Spectrom. **15**, 37 (2000).
[12] A. Bogaerts, E. Neyts, R. Gijbels, et al., Spectrochimica Acta Part B, **57**, 609 (2002).
[13] F. Massines, A. Rabehi, P. Decomps, et al., J. Appl. Phys., **83**, 2950 (1998).
[14] K. Akhtar, J.E. Scharer, S.M. Tysk, et al., Review of Scientific Instruments, **74**, 996 (2003).
[15] L. Ward, J. Appl. Phys. **33**, 2789 (1962).

[16] D. Balagangadhar and S. Roy, Computer Methods in Applied Mechanics and Engineering, **190**, 5465 (2001).
[17] S. Roy, B.P. Pandey, Physics of Plasmas, **9**, 4052 (2002).
[18] S. Roy and B.P. Pandey, Journal of Propulsion and Power, **19**, 964 (2003).
[19] S.M. Cooper, B.A. Cruden, M. Meyyappan, et al., Nano Letters, **4,** 377 (2004).
[20] J.N. Reddy, An Introduction to the Finite Element Method, McGraw-Hill Book Company, New York, 1984.

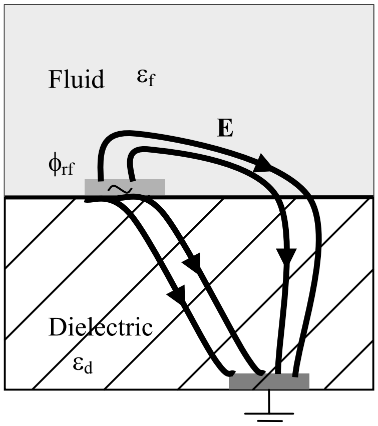

Figure 1. Schematic of the 2D simulation domain between RF induced dielectric barrier discharge.

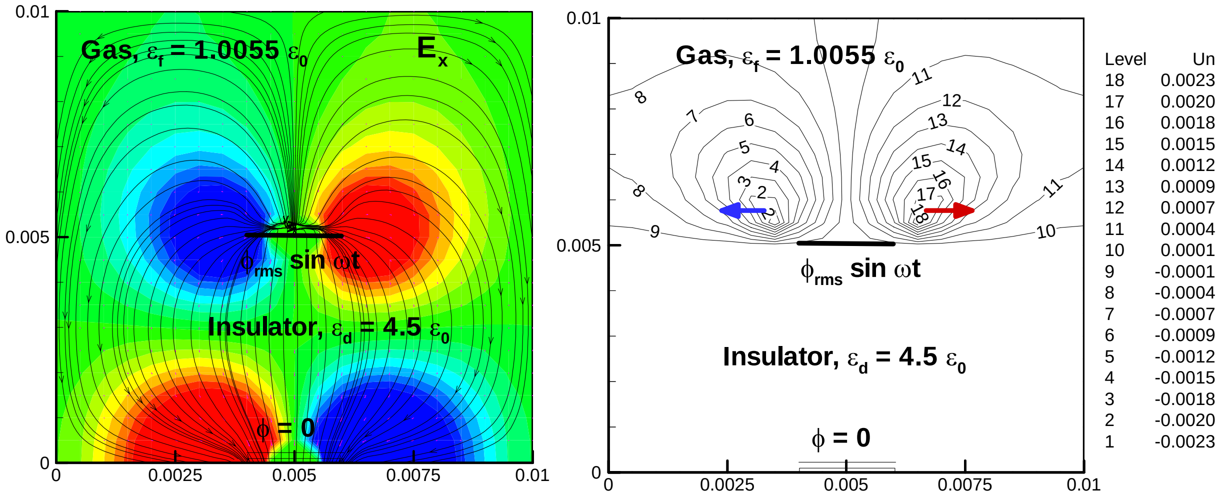

(a) (b)

Figure 2. Solution for symmetric configuration. (a) Computed axial electric field contours with embedded electric field lines. (b) Streamwise velocity contours calculated from the electric field in (a) shows counteracting flow field.

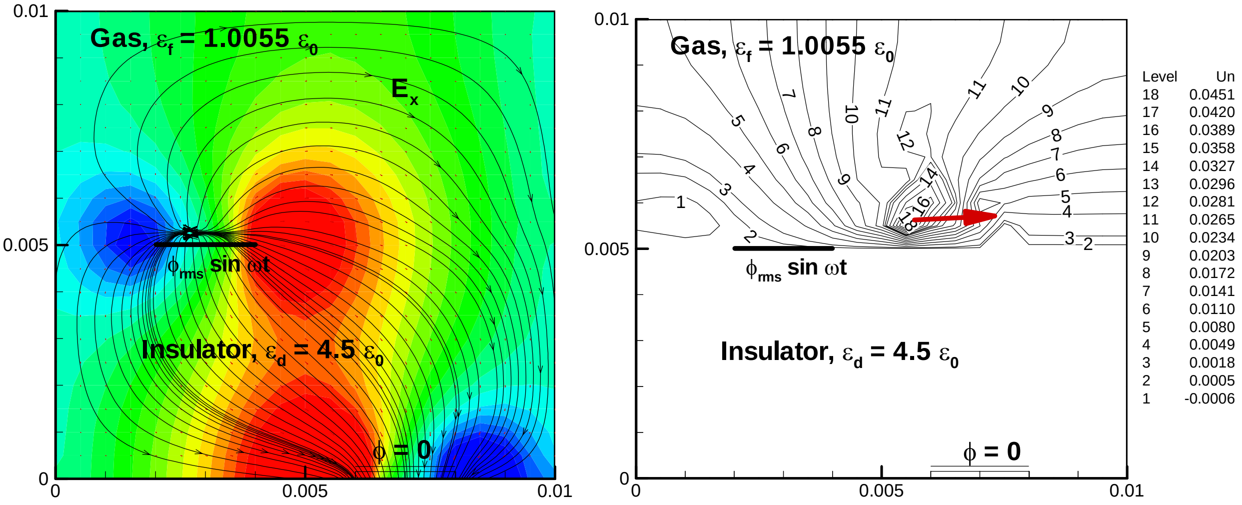

(a) (b)

Figure 3. Solution for asymmetric configuration. (a) Computed axial electric field contours with embedded electric field lines. (b) Streamwise velocity contours calculated from the electric field in (a) shows positive flow field.

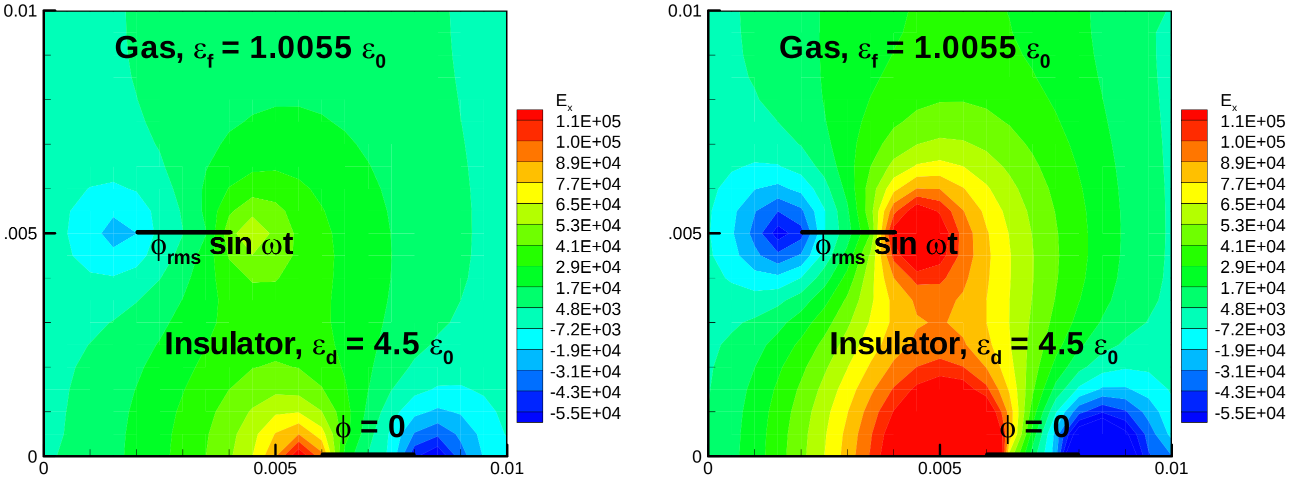

(a) ωt = π/5 rad (b) ωt = π/2 rad

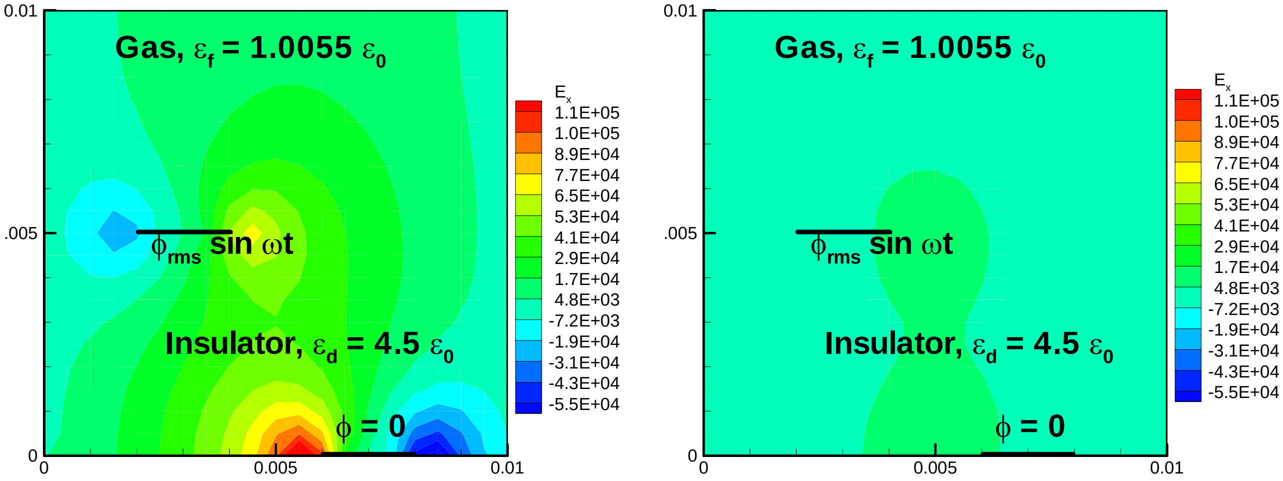

(c) ωt = 4π/5 rad (d) ωt = π rad

Figure 4. Time evolution of computed axial electric field (volts/cm) distribution in the computational domain.

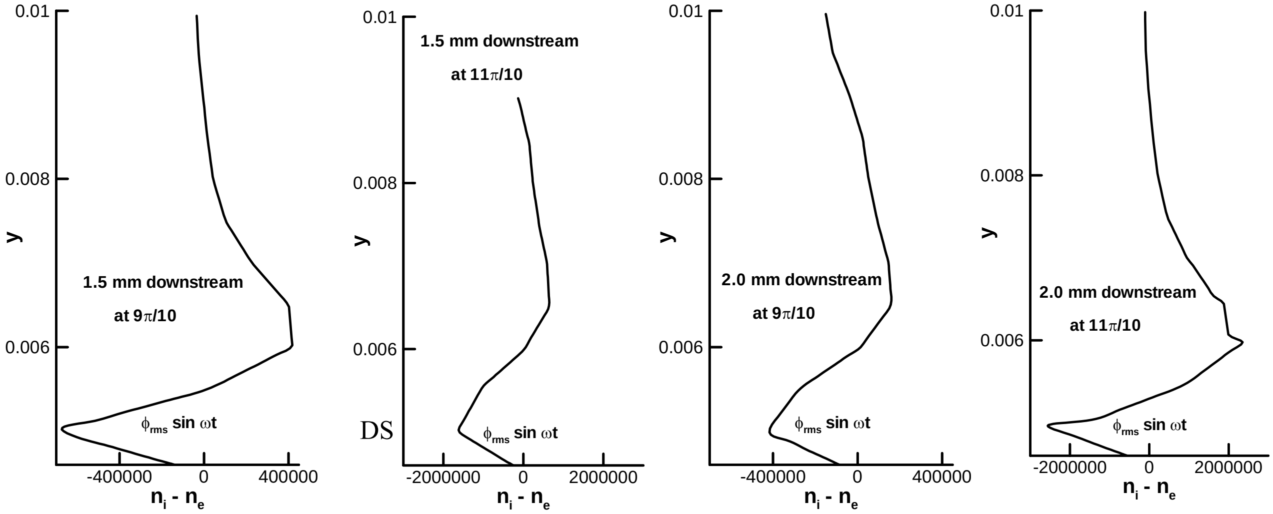

(a) (b) (c) (d)

Figure 5. Vertical crosssections downstream of the RF electrode showed negative charge accumulation at the surface of the dielectric (DS).

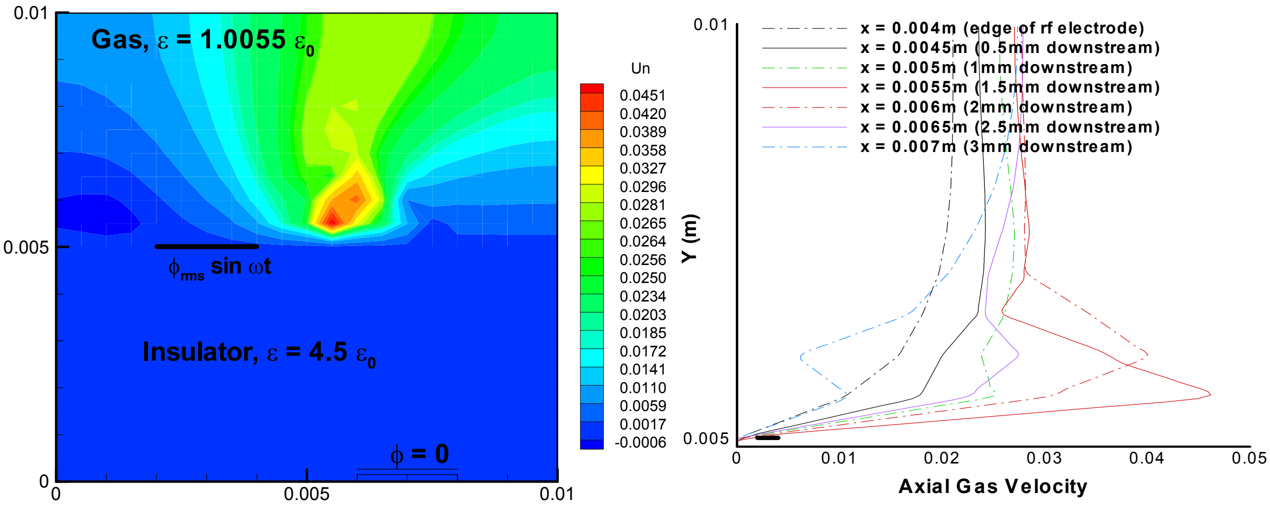

(a) (b)

Figure 6. (a) Contours of the streamwise velocity identify the location of highest momentum transfer, (b) Calculated streamwise component of the gas velocity distribution at different locations along the flow.